

www.acsami.org Research Article

Fully Biomass-Based Hybrid Hydrogel for Efficient Solar Desalination with Salt Self-Cleaning Property

Xiaojie Liu, Yanpei Tian, Yanzi Wu, Fangqi Chen, Ying Mu, Marilyn L. Minus, and Yi Zheng*



Cite This: ACS Appl. Mater. Interfaces 2021, 13, 42832-42842



ACCESS

Metrics & More



Supporting Information

ABSTRACT: Solar-driven interfacial steam generation provides an opportunity for solar harvesting and freshwater yield as a promising and eco-friendly technology. Here, we demonstrate a sustainable, nontoxic, and highly efficient fully biomass-based GG/CI hydrogel evaporator consisting of gellan gum (GG) hydrogel as the matrix and cuttlefish ink (CI) as the photothermal material. Induced by the ice-template method and freeze-drying method, vertically aligned microchannels are generated along the ice crystal growth direction. Efficient photothermal conversion is enabled by the natural black cuttlefish ink powder and enhanced by the light trapping effect within vertical microchannels. The hydrophilic



property of the gellan gum hydrogel and water capillary force in those microchannels boost water pumping to the top interfacial evaporation region. Effective rapid salt self-cleaning behavior is achieved due to the rapid ion diffusion within vertical microchannels. An evaporation rate of 3.1 kg m $^{-2}$ h $^{-1}$ under one sun irradiance is demonstrated by this fully biomass-based GG/CI hydrogel evaporator. This work offers a promising alternative for eco-friendly and sustainable freshwater generation with abundant natural biomasses.

KEYWORDS: biomass, gellan gum hydrogel, cuttlefish ink, solar evaporator, desalination

■ INTRODUCTION

The ever-increasing freshwater crisis brought about by rapid industrial development, fast-growing populations, and frequent water pollution accidents is one of the most pervasive issues affecting people worldwide. 1-3 Solar-driven steam generation, whereby solar energy is converted into thermal energy for generating purified water from seawater and sewage, is gaining considerable popularity to be an eco-friendly and sustainable path to mitigate water scarcity around the world because of its high photothermal conversion efficiency. 4-7 Tremendous research efforts are dedicated to boosting the energy efficiency of solar-driven interfacial evaporation, concentrating on ameliorating the system design, developing advanced photothermal materials to enhance solar absorption, achieving thermal management to realize effective heat localization, possessing fast salt rejection ability, and accelerating vapor diffusion. 8-16 To carry out a satisfactory water distillation performance, a solar-driven interfacial steam generation device should fulfill the following criteria: (1) high solar absorptance enabled by photothermal materials effectively converting solar irradiance into thermal energy; (2) water transportation channels rapidly pumping water to the interfacial evaporation surface and dissipating salt back to the bulk water; and (3) effective thermal insulation localizing heat at the interfacial evaporation region instead of losing to the bulk water.

Hydrogels, which are capable of possessing high water content ascribing to the hydrophilic functional groups in the polymer backbone and the three-dimensional polymeric networks, are emerging as a new materials platform for solar-driven steam generation.^{17–19} Notably, hydrogels can accelerate water evaporation mainly by reducing water evaporation enthalpy.^{20,21} Other advantages of hydrogels, e.g., managing heat distribution²² and tailoring evaporation surface²³ make it an ideal material for solar-driven desalination. Compared with other synthetic polymers that may exert negative impacts on the environment due to their ultralong degradation time, biomass is highly biocompatible and biodegradable after the lifespan, which has attracted enormous attention for the development of solar-driven evaporators owing to their biocompatibility, sustainability, and low production cost.^{24–30}

Gellan gum (GG), a nature-derived linear anionic polysaccharide produced in high yield, is widely used as a biocompatible, biodegradable, and hydrophilous fermentation material.^{31,32} As a green biopolymer material with nontoxicity,

Received: June 21, 2021 Accepted: August 20, 2021 Published: September 1, 2021





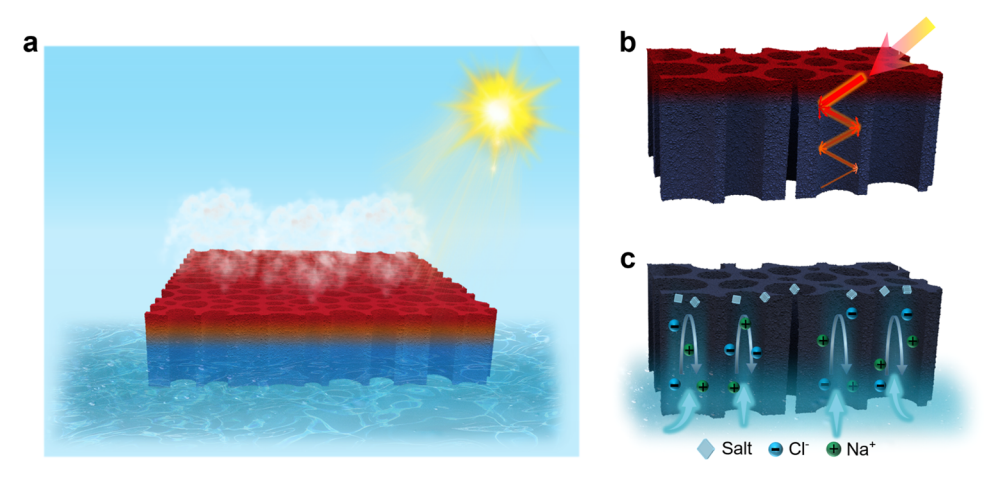


Figure 1. Design of the aligned porous GG/CI hydrogel evaporator. (a) Schematic illustration of the aligned GG/CI hydrogel evaporator for solar-driven desalination. Under solar irradiation, strong water evaporation can be powered by solar energy at the liquid/air interface. CI powders, which work as the photothermal material dispersed in the three-dimensional (3D) hydrophilic polymeric network of the GG hydrogel, harvest solar energy and convert it into thermal energy to heat the water all around the powders. (b) The vertically aligned channels in the GG/CI hydrogel can further lock up the sunlight (red arrows) and absorb it for vapor generation. (c) Schematic illustration of fast water transport and salt self-cleaning abilities in the aligned channels of the GG/CI hydrogel evaporator due to its naturally hydrophilic property and unidirectional channels.

widespread availability, and stability properties, GG has already achieved an important position in the biomedical industry for drug delivery and cell delivery 33,34 and in the food industry as a stabilizer and thickening agent. The GG aqueous solution undergoes a rapid thermally reversible gelation process from a disordered coil dimension at high temperature to a double helix structure at low temperature, and then a stable GG hydrogel is obtained after introducing the calcium ions (Ca²⁺), which promote more efficient gelation and aggregation of pairs of double helices by the chemical bonding between Ca²⁺ and gellan chains. Cuttlefish ink (CI) powder, consisting of natural melanin, is ultrablack and shows broadband solar absorption, rendering it a suitable ocean biomass-derived photothermal material. Furthermore, it is easy to disperse CI particles evenly into an aqueous solution of Supporting Materials arising from its hydrophilicity.³⁷

Here, a fully biomass-based GG/CI hydrogel evaporator consisting of gellan gum hydrogel and cuttlefish ink powder is demonstrated for high-efficiency solar-driven interfacial desalination. Assisted by the ice-template self-assembly and freeze-drying method, vertical microchannels are generated along the unidirectional ice crystal growth direction in the GG/CI hydrogel evaporator (Figure 1a). As the functional material with photothermal conversion effects, CI powders are uniformly distributed and embedded into the GG hydrogel to efficiently absorb solar irradiation and convert it into thermal energy, which is simultaneously enhanced by the multiple reflections of sunlight in the vertical microchannels (Figure 1b). The GG hydrogel continuously pumps adequate water to the top evaporation layer through vertical microchannels due to the swelling effect of hydrophilic function groups in polymer chains and enhanced capillary force within vertical channels (Figure 1c). Although the rapid vapor generation at the interfacial evaporation region causes a concentration gradient of salt along the aligned channels between the heating surface (higher salinity) and the bulk water (lower salinity), the aligned vertical channels which are fully swelled with lessconcentrated water provide a straight backward way to drive the ion diffusion down to the bulk water. The low thermal conductivity property of the GG/CI hydrogel makes it a

thermal barrier to restrict the solar heating effect to a narrow strip area near the air/liquid interface, which is conducive to the effective utilization of energy. To further enhance the heat localization effect, in this work, the GG/CI hydrogel evaporator is integrated into an evaporation device with an indirect contact water supply method, which consists of insulation foam (polyethylene (PE) foam) and a water pathway (cotton wipe). This design further restricts the conduction heat loss to the underlying bulk water and convection heat loss to the ambient air during the desalination process. This evaporation device has achieved an evaporation rate of 3.1 kg m $^{-2}$ h $^{-1}$ under one sun irradiation in a two-dimensional (2D) form.

■ EXPERIMENTAL SECTION

Materials. Gellan gum was purchased from Spectrum Chemical Mfg Corporation. Calcium chloride $(CaCl_2)$ and sodium chloride (NaCl) were purchased from Sigma-Aldrich. All chemicals were directly used as received without further purification. Pure cuttlefish ink powder was purchased from Fluxias GmbH Ltd., Germany. The cotton wipe used was supplied by Webril. The PE insulation foam was purchased from McMaster-Carr.

Preparation of the GG/CI Hydrogel. Typically, 2 wt % GG/CI hydrogel was prepared as follows: 0.4 g of cuttlefish ink powder was dispersed in 49 ml of deionized (DI) water and mixed adequately under alternative vigorous magnetic stirring and ultrasonication for 2 h at room temperature. After this uniform suspension was heated to 90 °C, 1 g of gellan gum powder was dissolved in the mixture, maintaining at 90 °C, still with vigorous magnetic stirring for 30 min until no visible suspended particles were observed. Subsequently, 0.03 wt % CaCl₂ as a crosslinking agent was added into the solution with continuous stirring for 10 min, when the temperature of the solution was reduced down to 55-60 °C. Then, the GG/CI hydrogel was obtained by casting the solution into a glass Petri dish (64 mm in diameter) and allowing it to cool down to room temperature for gelation. The obtained GG/CI hydrogel was placed on a copper platform, which is partially immersed by liquid nitrogen to achieve freezing. The frozen hydrogel was lyophilized at -85 °C until all solvent was completely removed, leaving a porous dark gray GG/CIbased cryogel. To get the GG/CI hydrogel with high water content, the cryogel was soaked into 0.03 wt % CaCl2 solution for 1 h, followed by flushing several times with DI water. The pure gellan gum hydrogel

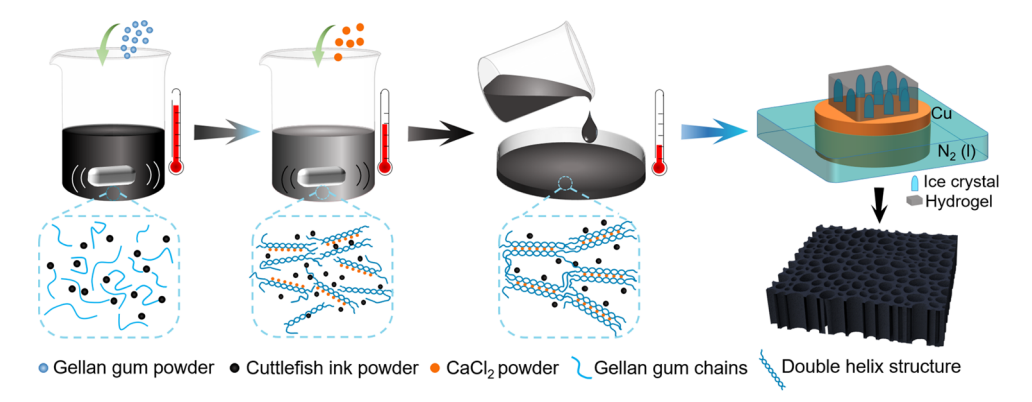


Figure 2. Schematic illustration of the fabrication process of the aligned GG/CI hydrogel.

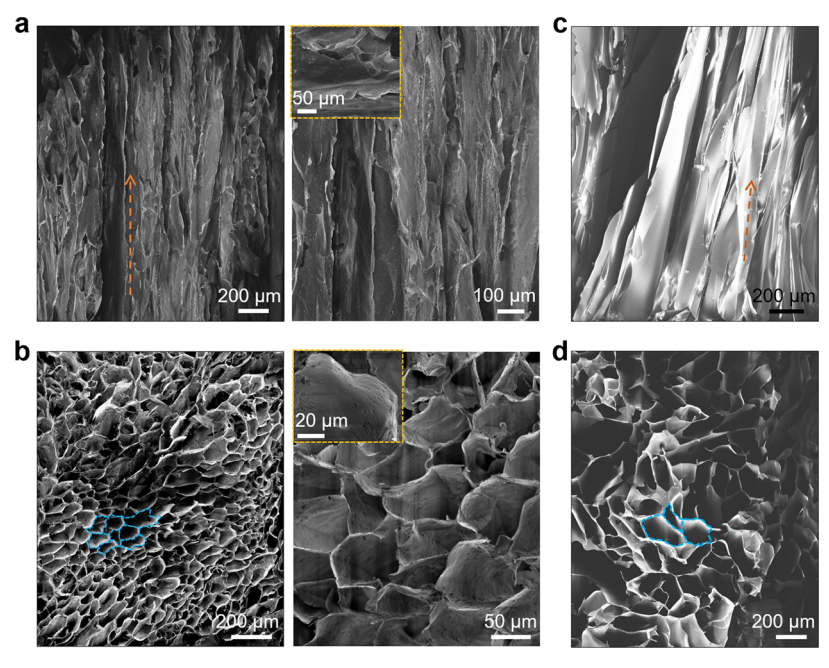


Figure 3. Structural characterization of the 2 wt % GG/CI aligned porous structure. (a) Scanning electron microscopy (SEM) images of the longitudinal section of the GG/CI porous structure with vertically aligned microchannels in different magnifications. In the left one, the orange dashed arrow indicates the direction of the vertically aligned channels. The inset with a yellow dashed border shows the embedded CI powders. (b) SEM images of the transverse section of the GG/CI aligned porous structure with numerous open channels in different magnifications. The blue dashed enclosures show the open channels for water transportation and vapor diffusion. The inset with a yellow dashed border shows CI powders attached to the channel walls of the structure. SEM images of (c) longitudinal section and (d) transverse section of the pure GG aligned porous structure. The orange dashed arrow denotes the direction of freezing. The blue dashed enclosures represent the cross sections of the open channels.

was fabricated following the same procedure without cuttlefish ink powder.

Solar Steam Generation Experiments. Steam generation experiments were carried out under a solar simulator (Newport, 94081A, class ABB), which supplies solar flux of 1 kW m⁻² with an optical filter for the standard AM 1.5G spectrum. Solar intensity at the position of the GG/CI hydrogel is measured by a TES 132 solar power meter when it is lower than 1 kW m⁻². While it is higher than one sun irradiation, the solar intensity is calibrated with a power sensor (Ophir FL250A-BB35). DI water and NaCl solutions with various concentrations are prepared and placed in a plastic beaker with an inside diameter of 48 mm. Before the crosslinking process, the dry GG/CI cryogel is cut into a thickness of 7 mm. The GG/CI hydrogel evaporator, tightly surrounded by PE foam with the same thickness, is placed on the PE foam, the center of which is penetrated by a strip of cotton wipe for supplying water. To accurately monitor the mass of the water remaining in the beaker, the evaporation device is placed on an electric balance (RADWAG, PS 1000.X2.NTEP) with a resolution of 0.001 g connected to a computer, which enables

recording of the real-time mass change. The real-time temperature is monitored by an infrared radiation camera (FLIR, A655sc).

Materials Characterizations. The reflectance spectra (UVvisible-near-infrared range: 300-2500 nm) are measured by the Iasco V770 spectrophotometer at an incident angle of 6° with the ISN-923 60 mm BaSO₄-based integrating sphere equipped with PMT and PbS detectors. The reflectance spectra are normalized by a PTFEbased reflectance standard. The reflectance spectra at different AOI were characterized using wedges of different angles at the sample port of the Jasco V770 spectrophotometer. The transmittance spectra (mid-infrared region: 2.5-20 μ m) are measured by the Jasco FTIR 6600 spectrometer at a normal incident angle regarding the background spectrum of a hydraulic pressed KBr film (20 psi). An Extech EC400 ExStik salinity meter is utilized to characterize the water quality of the collected water samples. Infrared images of samples were taken employing the FLIR A655C thermal camera at a resolution of 640×480 , with a 25° lens. The thermal conductivity of the samples was characterized by the Hotdisk TPS 2500 S. The contact angle of samples was measured by the SINDIN SDC-350 contact angle meter.

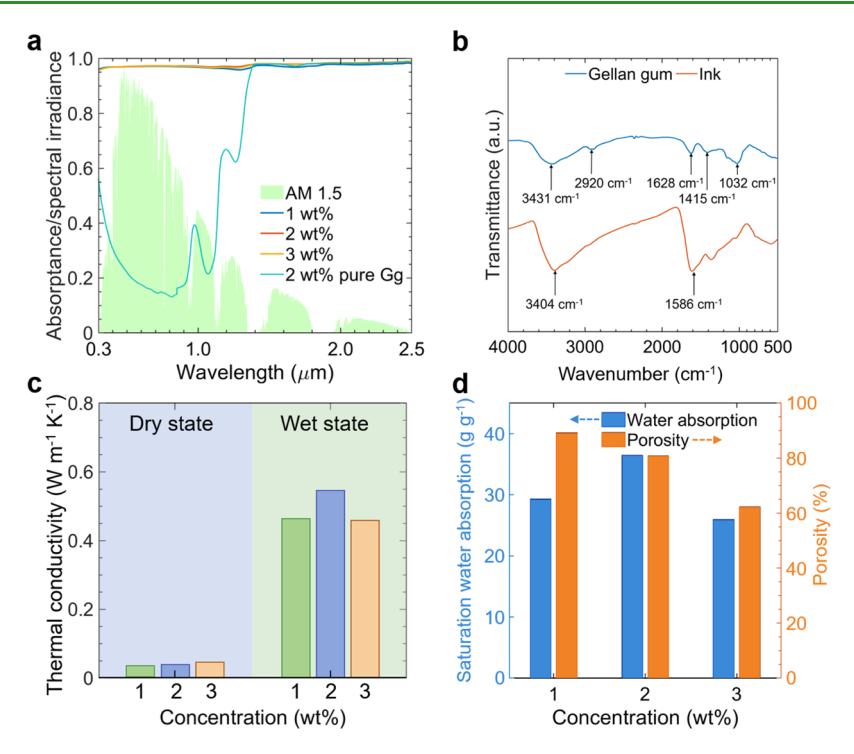


Figure 4. (a) Solar absorptance spectra of the hydrated GG/CI hydrogels with different concentrations of GG and a pure GG hydrogel displaying against the AM 1.5 spectral solar irradiance spectrum. (b) Fourier transform infrared (FTIR) spectra of GG powder (blue curve) and CI powder (orange curve) showing the corresponding chemical composition of GG and CI, respectively. (c) Thermal conductivity of different GG/CI hydrogels in the dry and wet states. (d) Saturated water absorption and porosity of GG/CI hydrogels with different concentrations of GG.

RESULTS AND DISCUSSION

Fabrication and Characterization of the GG/CI **Hydrogel.** The well-aligned porous GG/CI structure is processed through freeze-drying, also known as ice-templating, which has been applied extensively in the formation of versatile porous materials. The fabrication process of the aligned porous GG/CI cryogel is shown in Figure 2. The homogeneous black suspension is obtained by dispersing CI powder in DI water with vigorous stirring at room temperature. As a naturally occurring black pigment, melanin is the main constituent of CI, which has good light absorption across a broad spectrum of wavelengths. The aqueous solution of GG is obtained by completely dissolving GG powder in the black suspension at 90 °C with constant stirring, and the GG existing in solution is in a disordered coil conformation. During the cooling gelation process (from 90 °C to room temperature) of the GG/CI hydrogel, GG in the aqueous solution subsequently goes through a coil to double helix conformational transition first, and then the aggregation of helices which are directly bridged by divalent Ca²⁺ leads to the formation of strong junction zones, achieving the sol-gel transition. To form the aligned and ordered porous structure, the gel is placed on a copper platform, which is partially immersed by liquid nitrogen to achieve unidirectional freezing, after a lyophilization procedure in which the ice crystals inside the frozen gel are removed by sublimation of ice template; the GG/CI-based porous structure is obtained.

The pure GG-aligned porous structure displays a white color in a dry state due to the light scattering effect of the microstructures after lyophilization. After hydration, it becomes near-transparent because of the similar refractive index of water and GG (Figure S1a). The black color of the GG/CI aligned porous structure results from cuttlefish ink

powders which are distributed inside the GG polymeric network (Figure S1b). The main constituent of CI is melanin that is a natural black pigment with broadband light absorption over solar wavelengths. Ink powders with diameters mainly around 100–150 nm can efficiently absorb sunlight and convert it into heat, serving as effective photothermal materials (Figure S2). The hydrated GG/CI hydrogel presents a darker appearance visually than its dry state, becoming a suitable solar absorber for photothermal conversion.

By directional freezing of GG/CI gel and then lyophilizing, as shown in Figure 3a, well-aligned microchannels grow perpendicularly to the cold source. The spacing between the aligned walls is mainly located in the range between 70 and 100 µm. These well-aligned microchannels facilitate the fast water pumping from the bottom bulk water source to the top evaporating surface due to its capillary force and natural hydrophilic property. Moreover, upon exposure to sunlight, light can be conducted into the aligned channels and be fully absorbed for thermal energy generation. GG in the GG/CI hydrogel evaporator is used as a matrix, where CI powders are distributed in the channel walls of the GG hydrogel, and some of those powders adhere to the GG polymeric walls (Figures 3a, inset and S3). These black particles can convert the absorbed light to heat and conduct it to the surrounding water. The GG/CI hydrogel has open channels on its top surface, which benefits the vapor diffusion (Figures 3b and S4). The inset shows one of the open channels, and it can also serve as the light trapping holes to extend the sunlight absorption path. The pure GG-aligned porous structure displays smooth channel walls compared with the rough wall of the GG/CI hydrogel. There is no obvious change of dimension of microchannels between the GG and GG/CI hydrogel, illustrating that the introduction of CI powders has no impact

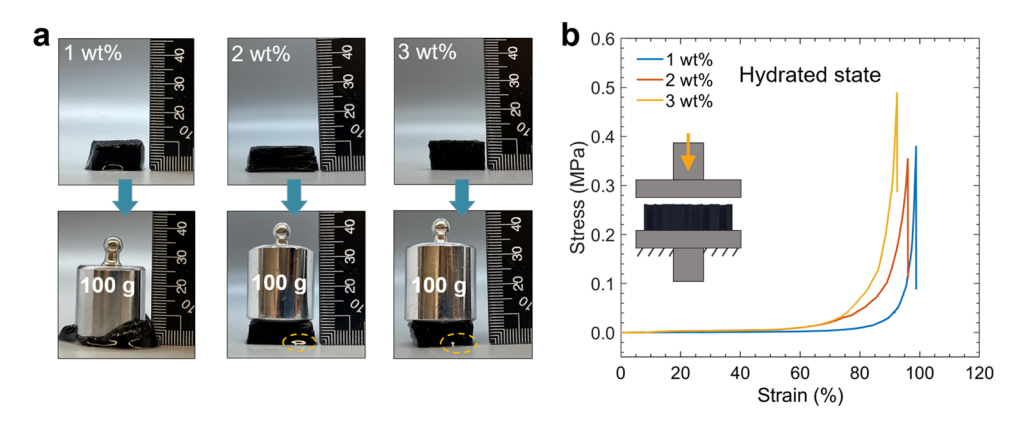


Figure 5. (a) Photographs exhibiting the comparison of mechanical strength of GG/CI the hydrogels with different concentrations of GG in the hydrated state. The yellow dashed circles show the water released when the weight is placed on the 2 and 3 wt % GG/CI hydrogels. (b) Compressive stress—strain curves of the GG/CI hydrogels with 1, 2, and 3 wt % concentrations in the hydrated states, respectively. The inset exhibiting the compression direction is parallel to the vertical microchannels in the hydrogels.

on the size of the channel during the lyophilization process (Figure 3c,d).

Solar Absorption, Heat Localization, and Tunable Water Transportation of the GG/CI Hydrogel Evaporator. Efficient solar absorption is one of the essential aspects for conducting a satisfactory evaporation performance of solardriven desalination. The GG/CI hydrogels exhibit an excellent solar absorptance of 0.97 in their hydrated states over the broadband spectrum of solar irradiance from 0.3 to 2.5 μ m (Figure 4a). The transmittance of the GG/CI hydrogel is negligible since hydrogel is thick enough to be opaque. The solar absorptance of the GG/CI hydrogels is significantly enhanced after the introduction of cuttlefish ink, attributing to the melanin in the cuttlefish ink and the porous structure of the polymeric network after freeze-drying. The aligned microchannels serve as light trapping wells that induce multiple reflections. Furthermore, the solar absorptance of the hydrated GG/CI hydrogels is angle-independent even at large incident angles, e.g., 60°, rendering it effectively absorb sunlight during most of the day and in most regions of the world (Figure S5).

To achieve a satisfactory evaporation performance, a continuously available water supply to the heating area is also essential for an evaporator. Fourier transform infrared (FTIR) spectra are provided to elucidate the chemical compositions of GG powder and CI powder (Figure 4b). The FTIR spectrum of only GG powder shows a broad absorption band around 3431 cm⁻¹ for -OH stretching vibration. The absorption peak at 2920 cm⁻¹ is caused by the C-H stretching of CH₂ groups. The peaks observed at 1628, 1415, and 1032 cm⁻¹ are ascribed to the stretching vibrations of COO (asymmetric), COO (symmetric), and C-O bonds, respectively.³⁹ The FTIR spectrum of only CI powder displays a broad absorption at 3404 cm⁻¹ resulting from the −OH groups of melanin, and a peak at 1586 cm⁻¹ comes from the symmetric COO⁻ stretching vibrations. 40 The hydrophilic feature of melanin due to the -OH groups enhances the water absorption of the GG/CI hydrogel. A dynamic water contact measurement of 2 wt % GG/CI hydrogel illustrates that the GG/CI hydrogel has a zero contact angle, and the water droplet is absorbed quickly after contact with the upper surface of the hydrogel (Figure S6). The strong water uptake ability and high porosity of the GG/CI hydrogels can be reflected in their thermal conductivities. As shown in Figure 4c, attributing to the porous structure of the GG/CI hydrogels, their thermal

conductivities are all below 0.045 W m⁻¹ K⁻¹ at dry states, indicating a large volume of air held in them. Because the void spaces are filled with water, the hydrated GG/CI hydrogels exhibit higher thermal conductivities than those of their dry states. The 2 wt % GG/CI hydrogel has the highest thermal conductivity of 0.54 W m⁻¹ K⁻¹ owing to its highest water absorption capacity (Figure 4d). The tunable water absorption ratio of the GG/CI hydrogel is another advantage for solardriven desalination applications. The saturation water absorption ratio of the GG/CI hydrogel W is determined by: $W = (m - m_0)/m_0$, where m represents the mass of the hydrogel after fully absorbing water, and m_0 is the mass of the initial dry aligned porous structure. The detailed measurement process of saturation water absorption ratio is provided in the Supporting Information. As shown in Figure 4d, the saturation water absorption ratio varies according to the GG concentrations. The GG/CI hydrogels with a 2 wt % GG concentration show the highest saturation water absorption ratio of 37 g g⁻¹. The high water content for the hydrogel indicates the large free space existing in the 3D polymeric network, which means the high porosity of the porous structure as well. Compared to the 2 wt % GG/CI hydrogel with 81% porosity, the water uptake ability of 3 wt % GG/CI hydrogel, with a denser microstructure, gets lower as the porosity decreases to 62%. Although the 1 wt % GG/CI hydrogel has the highest porosity, it is challenging for it to maintain the water inside the structure in a steady and sustained way due to its weak strength. The mechanical strength of the hydrogel foam is consequential for practical industrial implementations (Figure 5). To evaluate the mechanical strength of the hydrogels with different initial GG concentrations, a 100 g weight is placed on top of these hydrated hydrogels (Figure 5a). The hydrogel with 1 wt % GG collapses immediately when the weight is put on, but the hydrogels with 2 and 3 wt % GG can withstand the weight without deformation, releasing little water. As shown in Figures 5b, S7, and S8, the compressive stress-strain curves of the GG/CI hydrogels with concentrations of 1, 2, and 3 wt % are measured in dried and hydrated states, respectively, which quantitatively demonstrate the mechanical properties of the GG/CI hydrogels. The compression direction is parallel to the vertical microchannels in the hydrogels (Figure 5b, inset). For both the dried and hydrated states of the GG/CI hydrogels, their fracture stress is all above 0.33 MPa, indicating that they

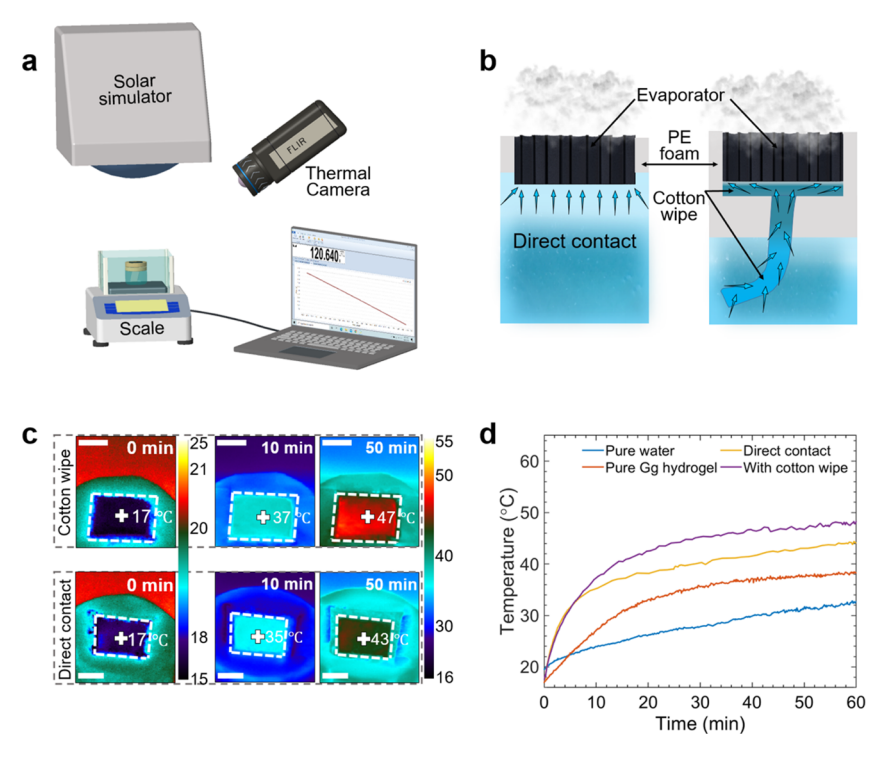


Figure 6. (a) Schematic illustration of the setup for solar desalination experiment involving the solar simulator, electrical balance, evaporation device, infrared camera, and PC. (b) Schematic showing the water supply methods of direct contact with water (left) and a cotton wipe as a water path (right). (c) Infrared (IR) images exhibiting the temperature distribution of the evaporator's top surface with two different water supply methods: (top) the cotton wipe serving as the water path, (bottom) the GG/CI hydrogel directly contacting the water. (d) Central surface temperature evolutions of the GG/CI hydrogels with different water supply methods, pure GG hydrogel, and pure water, respectively.

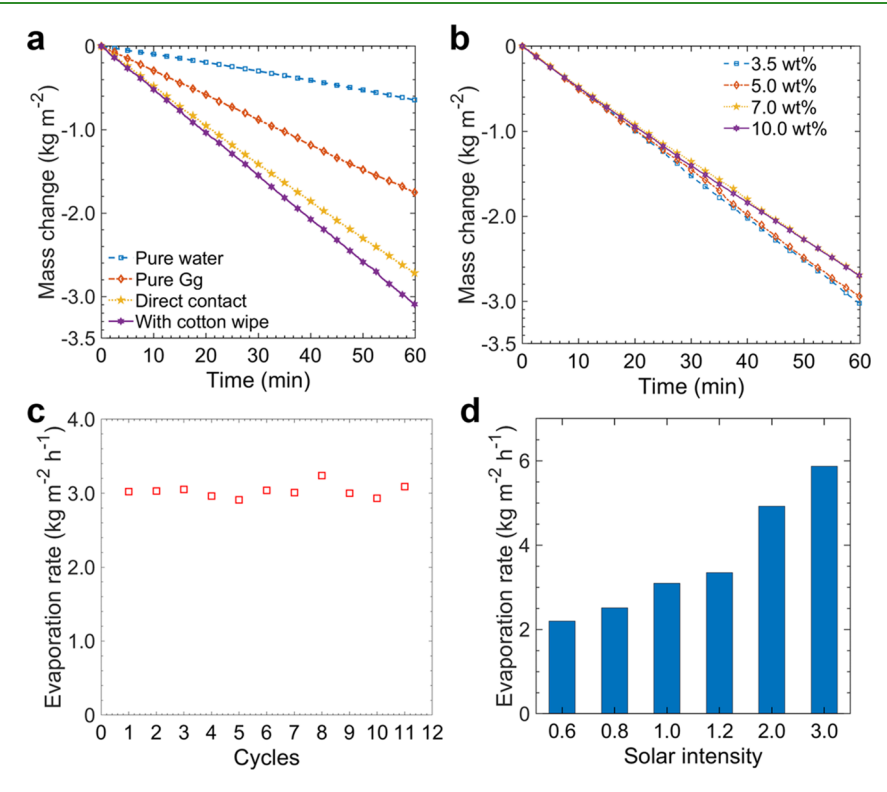


Figure 7. (a) Mass changes of water for the GG/CI hydrogel evaporator in different water supply methods under one sun irradiation, with pure water as control. (b) Mass changes of solutions with various salinities for the GG/CI hydrogel evaporator. (c) Evaporation rates of the GG/CI hydrogel evaporator for 11 cycles under one sun illumination. (d) Evaporation rates of the GG/CI hydrogel evaporator under different solar intensities.

possess a good mechanical strength for real-life applications. The compression strengths for the hydrated GG/CI hydrogels with different concentrations are higher than 0.35 MPa, which are recorded at fracture strains greater than 92%, allowing for high deformability of the hydrogels.

Solar Desalination Performance of the GG/CI Hydro**gel Evaporator.** The solar-driven desalination performance of the GG/CI hydrogel evaporator is systematically investigated with the experimental setup as schematically depicted in Figure 6a. The water evaporation rate of the GG/CI hydrogel evaporator is evaluated by recording the mass change of the evaporation device over time, and its photothermal response is investigated by the infrared thermal camera. The ambient temperature fluctuates around 19.5 °C, and the humidity keeps at around 55% (Figure S9a,b). Different from the direct contact water supply method, the evaporator is placed directly in the water and floats on the water surface. Here, water transportation from the bulk water to the upper GG/CI hydrogel evaporator is achieved via a cotton wipe strip, which is supported by a PE foam (Figures 6b and S9c,d). The water supply through the cotton wipe effectively minimizes the downward conductive heat dissipation to the bulk water by eliminating the area in direct contact with the bulk water. Moreover, ascribing to the hydrophilicity and porous structure of the cotton wipe, the confined water supply method via cotton wipe can continuously deliver water to the evaporator driven by the strong capillary force during the evaporation process (Figure S10). Due to the low thermal conductivity of PE foam $(0.044 \text{ W m}^{-1} \text{ K}^{-1})$ and wet cotton wipe (0.56 W)m⁻¹ K⁻¹), the GG/CI hydrogel evaporation device effectively localizes absorbed heat within the GG/CI hydrogel evaporator to increase its stagnation temperature for fast evaporation. To restrict the heat loss from the GG/CI hydrogel evaporator, as a heat reservoir to the surrounding environment, the hydrogel evaporator was surrounded by the PE foam, and that ensures that the upper surface of the evaporator is the only exit for the generated vapor to diffuse out.

Figure 6c shows the surface temperature distributions of the GG/CI hydrogel evaporators within 50 min of the initial operation. With the same initial temperature of bulk water at 20 °C, the central surface temperature of the GG/CI hydrogel evaporator with a cotton wipe water supply stabilizes at 47 °C, which is 4 °C higher than that with the direct contact water supply method under one sun. Owing to the helpful heat localization effects of PE foam and cotton wipe, the pure GG hydrogel evaporator, without CI powder as the photothermal material, reaches a stable central surface temperature of 38 °C, while the central surface temperature of pure water is stabilized at 32 °C. Due to the fast photothermal conversion ability and the low thermal conductivity induced by the aligned porous structure, the GG/CI hydrogel evaporators with both two water supply methods demonstrated rapid temperature response when the sunlight hits them (Figure 6d). The typical time-dependent mass change curves are shown in Figure 7a with DI water as bulk water, and the real-time mass of the evaporation device is recorded after 30 min of exposure to light illumination. Under one sun irradiation, the evaporation rate of pure water is only 0.64 kg m⁻² h⁻¹. After the addition of a 7 mm thick 2 wt % pure GG hydrogel as an evaporator which is equipped with a cotton wipe and PE foam, the evaporation rate reaches 1.75 kg m⁻² h⁻¹, which is 2.7 times that of pure water. The evaporation rate further significantly increases to 3.1 kg $m^{-2} h^{-1}$ after introducing the CI powder into the GG hydrogel

as the photothermal material for heat generation, which is 4.84 times that of pure water, benefiting from the reduction of vaporization enthalpy for water in the hydrogel. To quantitatively prove the decrease of vaporization enthalpy of water in the hydrogel during the evaporation process, differential scanning calorimeter (DSC) and the dark environment tests at the equilibrium temperature were conducted (Table S1, Figures S11 and S12). In addition, the GG/CI hydrogel evaporator with direct contact water supply method yielded a slower evaporation rate of 2.7 kg m⁻² h⁻¹ compared with that of using the PE foam as a thermal insulator and the cotton wipe as a water pathway.

The solar-driven desalination performance of the GG/CI hydrogel evaporator in solutions with various salinities is further evaluated to examine its broad applicability in brine source (Figure 7b). For a 3.5 wt % NaCl solution, the GG/CI hydrogel evaporator shows an evaporation rate of 3.0 kg m⁻² h⁻¹, which is similar to the performance in DI water. Even utilizing a high salinity (10 wt % NaCl solution), it still yielded an evaporation rate of 2.7 kg m⁻² h⁻¹, resulting from its continuous replenishment of water and fast salt drainage capability within the vertical microchannels. The tests for evaporation rates of the GG/CI hydrogel evaporator in the 3.5 wt % NaCl solution were repeated 11 times to demonstrate the stability of the evaporation performance, and results are shown in Figure 7c. The evaporation rates slightly fluctuated in the range of 2.9-3.2 kg m⁻² h⁻¹. Solar irradiance varies with different times of the day, and the concentrated sunlight can highly boost the evaporation performance. To investigate the working performance of the GG/CI hydrogel evaporator under nonstandard solar irradiance, the evaporation rates of the GG/ CI hydrogel evaporator under different solar intensities from 0.6 to 3.0 kW m⁻² were tracked (Figure 7d). Under weak sunlight, the GG/CI hydrogel evaporator still yielded evaporation rates of 2.2 and 2.5 kg m⁻² h⁻¹ under 0.6 and 0.8 kW m⁻², respectively. For a solar intensity of 3.0 kW m⁻², the GG/CI hydrogel evaporator can achieve an evaporation rate of 5.9 kg m⁻² h⁻¹. The evaporation performance of the GG/CI hydrogel evaporator ensures that it can work under different solar intensities and can be used even for concentrated solar desalination applications.

Salt Self-Cleaning Performance of the GG/CI Hydrogel Evaporator. Excellent salt self-cleaning performance is another premise for efficient solar-driven desalination. The accumulated salt crystal on the top surface of the GG/CI hydrogel evaporator will severely impede sunlight absorption and vapor diffusion. Once the massive salt crystals formed on the surface or inside the hydrogel, they will clog vertical salt drainage channels and water transportation paths of the GG/ CI hydrogel evaporator, hindering the replenishment of water pumped to the top evaporation surface. Therefore, salt selfcleaning is a key factor for the continuous solar desalination process. The strong capillary force along the aligned microchannels and naturally hydrophilic property of the GG/CI hydrogel evaporator ensure sufficient water supply and shorten the salt diffusion path in the hydrogel to prevent salt accumulation. Usually, there is no visible salt accumulation phenomenon on the surface of the GG/CI hydrogel evaporator with 3.5 wt % NaCl solution under one sun illumination. To validate the strong salt self-cleaning ability of the GG/CI hydrogel evaporator, we mimicked the salt crystal growth process on the top surface of the GG/CI hydrogel evaporator under concentrated sunlight. As shown in Figure 8a, the

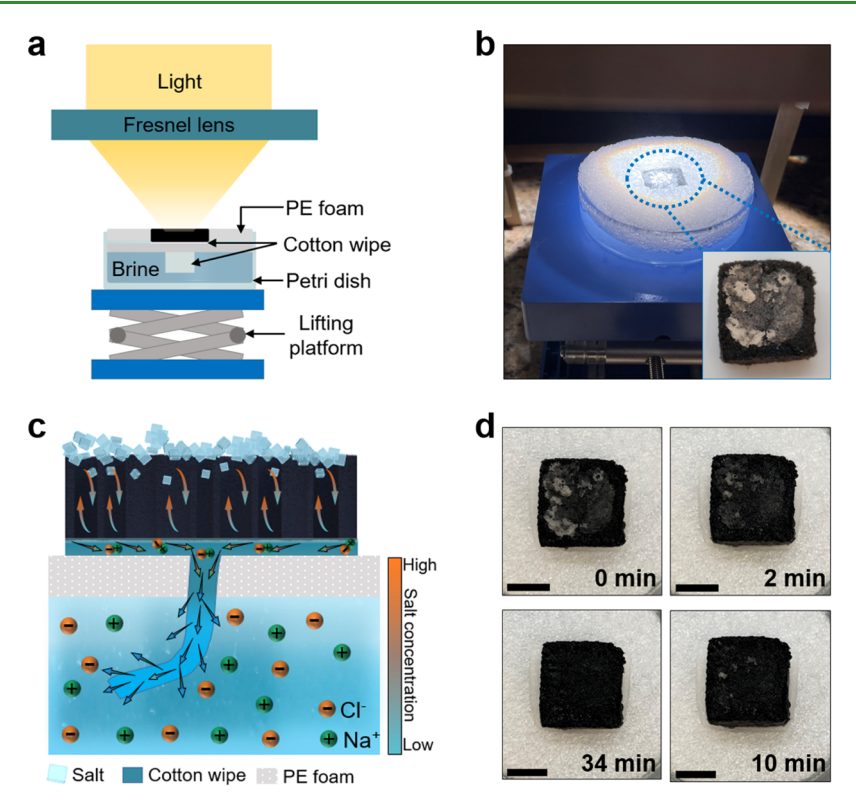


Figure 8. (a) Schematic showing the experimental setup for salt accumulation under concentrated sunlight. (b) Photograph of the GG/CI hydrogel evaporator under 8 sun irradiation. Inset elucidating the top view of salt accumulation on the top surface of the GG/CI hydrogel evaporator after 30 min under 8 sun irradiation with 7.0 wt % NaCl solution. (c) Schematic illustrating the working process of salt self-cleaning for GG/CI hydrogel evaporator in a 3.5 wt % NaCl solution. The arrows indicate the salt exchange between the GG/CI hydrogel and bulk water. (d) Time-lapse photographs of the salt dissolving process on the top surface of the GG/CI hydrogel evaporator. The scale bars are 1 cm.

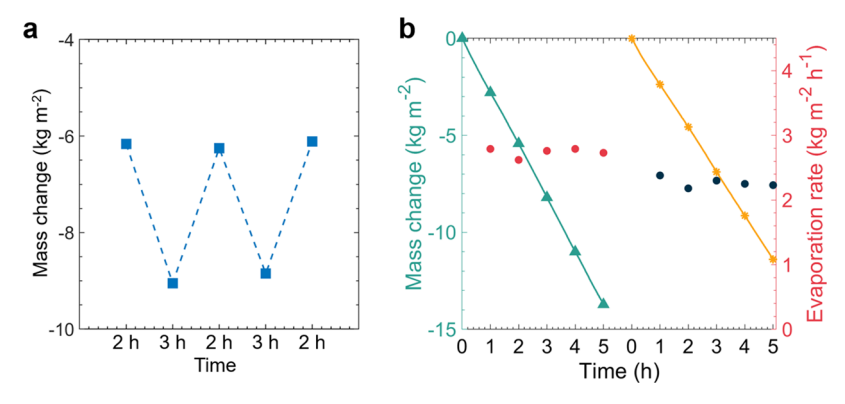


Figure 9. (a) Mass changes of the GG/CI hydrogel evaporator for a duration test under one sun irradiation with a 3.5 wt % NaCl solution. (b) Mass changes of the GG/CI hydrogel evaporator with vertical microchannels (solid green curve) and with randomly porous structures (solid yellow curve) during a 5 h desalination experiment with a 10 wt % NaCl solution as the bulk water.

experimental setup consists of a solar simulator to provide the light source, a Fresnel lens to concentrate sunlight, a lifting platform to support the evaporation device and adjust the distance between the Fresnel lens and the evaporator, and an evaporation device. To accumulate more salt on the evaporator in a short time, the experiment was conducted under 8 suns (8 kW m⁻²) irradiation with 7 wt % NaCl solution as bulk water. When the light is on, the focus of concentrated light covers the evaporation surface, and the saltwater intensively and continuously evaporates away from the upper surface. As the strong evaporation process was going on, the concentration of water present in the heating area was increasing, and salt crystals then gradually formed (Figure 8b). After 30 min, most

of the top surface area of the GG/CI hydrogel evaporator was covered by the accumulated salt (Figure 8b, inset).

To simulate the working state of this GG/CI hydrogel evaporator with massive salt accumulation in the evening, the hydrogel was placed on 3.5 wt % NaCl solution, which was connected by the cotton wipe (Figure 8c). Without strong vapor generation, the salts accumulated on the upper surface started to dissolve in the water with lower salinity and then diffused downward to the bulk water through the microchannels. The accumulated salts increase the brine concentration within the top small region of the GG/CI hydrogel evaporator. The concentration difference between the high salt concentration region and the bulk water causes the diffusion and convection of salt down along the vertical micro-

channels.^{8,26,29} This driven force induced by the salt potential difference between the top and bottom regions of the GG/CI hydrogel evaporator facilitates the salt diffusion within the interior vertical microchannels. The cotton wipe provides a drainage pathway for the accumulated salts. Time-lapse images record the salt dissolving process on the top surface of the GG/CI hydrogel evaporator (Figure 8d). It is elucidated that most of the salts dissolved in the first 2 min, which indicates the fast salt self-cleaning capability of the GG/CI hydrogel evaporator. After 34 min, all of the accumulated salts are completely dissolved, illustrating the excellent salt rejection performance of the GG/CI hydrogel evaporator. A continuous desalination test of GG/CI hydrogel evaporator with 3.5 wt % NaCl solution for 12 h was conducted to demonstrate the durability of the evaporator. Under long-term light illumination, the conductive thermal dissipation via the cotton wipe from the evaporator to the bulk water and the radiative thermal transfer from surroundings to the bulk water will inevitably heat the bulk water. To eliminate the heat effect for bulk water and keep water salinity constant, the bulk water was replaced every 2 or 3 h. Results are shown in Figures 9a and S13, and the evaporation rate still maintained at 3.0 kg m⁻² h⁻¹ throughout the test.

Better saturation water absorption capacity and faster salt self-cleaning process are two advantageous parameters of the GG/CI hydrogel evaporator with vertically aligned channels over that with randomly porous structures. The overall solar absorptance of the GG/CI hydrogel evaporator with randomly porous structures is 0.97, which is consistent with that of the hydrogel with vertical channels (0.972) (Figure S14a,b). The hydrogel evaporator with vertical channels has no obvious advantage over the randomly porous structures in terms of light absorption. This is because the CI powder is ultrablack, which is enough to render an approaching unity solar absorptance when it is mixed uniformly with the GG hydrogel. Besides, both the aligned porous structure and the randomly porous structure have rough outer surfaces, which are conducive to trapping light. The thermal conductivities and the saturation water absorption capacities of the GG/CI hydrogel evaporators with different structures were measured. The 2 wt % GG/CI hydrogel with randomly porous structures shows a low thermal conductivity that is similar to the hydrogel evaporator with vertical channels in the dry state (Figure S14c). However, in the hydrated state, the 2 wt % GG/CI hydrogel evaporator with randomly porous structures has a thermal conductivity of 0.28 W m⁻¹ K⁻¹, which is lower than that of the 2 wt % GG/CI hydrogel evaporator with vertical channels (0.55 W m⁻¹ K⁻¹). Figure S14d demonstrates the saturation water absorption capacity, the ratio of the weight of absorbed water to the weight of the dried sample for GG/CI hydrogels with different structures. The saturation water absorption rate of the 2 wt % GG/CI hydrogel evaporator with randomly porous structures (26.02 g g⁻¹) is lower than that of the structures with vertical channels (36.48 g g⁻¹). A higher water absorption capacity indicates a higher thermal conductivity, filling with a large amount of water. This also illustrates the advantage of using the unidirectional icetemplate freeze-drying to generate vertical channels since the vertical channels are better at absorbing more water, which is a key point of enhancing the water evaporation rate. Due to the relatively low thermal conductivity of the GG/CI hydrogel evaporator with randomly porous structures (Figure S14c), its temperature response upon exposure to solar irradiation is

faster than that of the hydrogel evaporator with vertical channels. As shown in Figure S14e, the central surface temperature of the GG/CI hydrogel evaporator with randomly porous structures rises more quickly than that of the GG/CI hydrogel evaporator with vertical channels within the initial 20 min. The stabilized temperature of randomly porous structures is also slightly higher than that of vertical channels. The faster thermal response rate and the higher stabilized temperature for the randomly porous structures can be attributed to two points: First, the hydrated 2 wt % GG/CI hydrogel with porous structure has lower thermal conductivity compared with those of hydrogels with aligned vertical channels in hydrated states, which helps reduce downward conductive heat loss and limit the heat in the upper surface. Second, according to the lower values of thermal conductivity and saturation water absorption capacity for porous GG/CI hydrogel in the hydrated state, we can infer that the water absorption ability of 2 wt % GG/CI hydrogel is a little weaker than that with vertical channels. Although the randomly porous structure shows better heat localization effects than the structure with vertical channels, its slower saturation water absorption rate limits its evaporation rate. As shown in Figure S14f, the GG/ CI hydrogel evaporator with vertical channels shows a water evaporation rate of 3.1 kg m⁻² h⁻¹, which is higher than that of the GG/CI hydrogel evaporator with porous structures. Therefore, it is confirmed that the structure with vertical channels is more advantageous than the random porous structures in enhancing the water evaporation rate for the GG/ CI hydrogel. Another advantageous point is the faster salt selfcleaning property of the structure with vertically aligned channels, which may be derived from the low tortuosity of the vertical microchannels (Figure S15). The abundant and vertically aligned microchannels ensure the salt transportation from the high salt concentration evaporating surface to the bulk water along the shortest path by diffusion and convection, endowing the vertically aligned microchannels with better salt rejection performance. To examine this, 0.5 g salt crystals were directly placed on the top surface of the GG/CI hydrogel evaporators with vertical microchannels (18 mm \times 19 mm \times 7 mm) and randomly porous structures (18 mm \times 19 mm \times 7 mm) simultaneously, and the salt rejection processes were recorded with a camera (Figure S16). The bulk water is a 3.5 wt % NaCl solution. Salt crystals on the surface of the hydrogel evaporator with vertical microchannels dissolve within 8 h, while it takes 10 h for salt crystals on the surface of the hydrogel with randomly porous structures to dissolve. Better salt rejection performance is of great significance to achieve a higher water evaporation rate. Moreover, a 10 wt % NaCl solution is selected to demonstrate the water evaporation rate of these two hydrogel evaporators with different inner microstructures for a continuous 5 h evaporation test under one sun (Figure 9b). Even though there is no salt crystalized on the surfaces of these two hydrogel evaporators, the hydrogel evaporator with vertical microchannels yields a higher water evaporation rate (2.75 kg m⁻² h⁻¹) than that of the hydrogel evaporator with randomly porous structures $(2.25 \text{ kg m}^{-2} \text{ h}^{-1})$. This verifies the advantage of the structure with vertical microchannels over the random porous structure.

CONCLUSIONS

In summary, a fully biomass-based GG/CI hydrogel evaporator with well-aligned microchannels is demonstrated to yield an evaporation rate of 3.1 kg m $^{-2}\,h^{-1}$ in a 2D evaporation surface

under one sun irradiance. Fast water evaporation rates are attributed to high solar absorptance, rapid water transportation, efficient salt self-cleaning performance, and enhanced heat localization. An approaching unity solar absorptance is induced by the introduction of cuttlefish ink as the photothermal material and the extended multiple reflections within those vertical light trapping channels. Fast rapid water transportation results from the hydrophilic property of the gellan gum hydrogel, which is enhanced by the capillary force in unidirectional water supply channels, pumping water to the top interfacial evaporation region. Quick ion diffusion into the sufficient water pumped to the evaporation region leads to effective salt rejection to prevent salt accumulation, ensuring continuous and rapid solar desalination. The porous structure of the GG/CI hydrogel evaporator, owing to the ice crystal growth in the hydrogel polymeric network, contributes significantly to its low thermal conductivity and thus efficiently confines thermal energy within the water/air interfacial evaporation region. Moreover, the indirect water supply method employing PE foam as a thermal insulator and a cotton wipe as a water transportation path helps to effectively localize heat within the hydrogel evaporator to power fast water evaporation. Taking advantage of the abundant and sustainable raw materials, like gellan gum and cuttlefish ink, and high freshwater yields, this GG/CI hydrogel evaporator can be a promising alternative for environmentally friendly freshwater production for different water sources, such as polluted water and seawater.

ASSOCIATED CONTENT

Supporting Information

The Supporting Information is available free of charge at https://pubs.acs.org/doi/10.1021/acsami.1c11636.

Photographs of pure GG-based and GG/CI-based aligned porous structures in the dried and hydrated states (Figure S1); SEM images of cuttlefish ink powders and the statistical analyses of the diameters of powders (Figure S2); SEM images showing the longitudinal section and transverse section of GG/CI aligned porous structures, respectively (Figures S3 and S4); average solar absorptance of the GG/CI hydrogels across different angles of incidence from 0 to 60° in the hydrated state (Figure S5); dynamic contact angle of the 2 wt % GG/CI hydrogel. (Figure S6); compressive stress-strain curves of the GG/CI hydrogels (Figure S7); SEM images of the transverse section of a GG/CI hydrogel with different concentrations (Figure S8); environment conditions of darkroom for the evaporation tests (Figure S9); SEM images of cotton wipe used as a water path (Figure S10); experimental setup for the dark environment tests with the surface temperature at 49 °C (Figure S11); experiment results for dark environments (Table S1); DSC curves of pure water and the water in the hydrogel (Figure S12); mass changes of a GG/CI hydrogel evaporator for a 12 h test under 1 sun irradiation (Figure S13); SEM images of the GG/CI hydrogel with randomly porous structure and the thermal response property of it (Figure S14); schematic illustrating the salt rejection process of the GG/CI hydrogel with different porous structures (Figure S15); time-lapse images showing the self-cleaning property

difference of the GG/CI hydrogel evaporators (Figure S16) (PDF)

AUTHOR INFORMATION

Corresponding Author

Yi Zheng — Department of Mechanical and Industrial Engineering, Northeastern University, Boston, Massachusetts 02115, United States; orcid.org/0000-0003-4963-9684; Email: y.zheng@northeastern.edu

Authors

- Xiaojie Liu Department of Mechanical and Industrial Engineering, Northeastern University, Boston, Massachusetts 02115, United States
- Yanpei Tian Department of Mechanical and Industrial Engineering, Northeastern University, Boston, Massachusetts 02115, United States; ⊚ orcid.org/0000-0003-4181-9517
- Yanzi Wu Department of Mechanical and Industrial Engineering, Northeastern University, Boston, Massachusetts 02115, United States
- Fangqi Chen Department of Mechanical and Industrial Engineering, Northeastern University, Boston, Massachusetts 02115, United States
- Ying Mu Department of Mechanical and Industrial Engineering, Northeastern University, Boston, Massachusetts 02115, United States
- Marilyn L. Minus Department of Mechanical and Industrial Engineering, Northeastern University, Boston, Massachusetts 02115, United States

Complete contact information is available at: https://pubs.acs.org/10.1021/acsami.1c11636

Notes

The authors declare no competing financial interest.

ACKNOWLEDGMENTS

This project is supported by the National Science Foundation through Grant number CBET-1941743.

■ REFERENCES

- (1) Rosa, L.; Chiarelli, D. D.; Rulli, M. C.; Dell'Angelo, J.; D'Odorico, P. Global Agricultural Economic Water Scarcity. *Sci. Adv.* **2020**, *6*, No. eaaz6031.
- (2) Ma, T.; Sun, S.; Fu, G.; Hall, J. W.; Ni, Y.; He, L.; Yi, J.; Zhao, N.; Du, Y.; Pei, T.; Cheng, W. Pollution Exacerbates China's Water Scarcity and Its Regional Inequality. *Nat. Commun.* **2020**, *11*, No. 650.
- (3) Richter, B. D.; Bartak, D.; Caldwell, P.; Kyle Davis, F.; Debaere, P.; Hoekstra, A. Y.; Li, T.; Marston, L.; McManamay, R.; Mekonnen, M. M.; Ruddell, B. L.; et al. Water Scarcity and Fish Imperilment Driven by Beef Production. *Nat. Sustainability* **2020**, *3*, 319–328.
- (4) Xu, Z.; Zhang, L.; Zhao, L.; Li, B.; Bhatia, B.; Wang, C.; Wilke, K. L.; Song, Y.; Labban, O.; Lienhard, J. H.; Wang, R.; et al. Ultrahigh-Efficiency Desalination via A Thermally-Localized Multistage Solar Still. *Energy Environ. Sci.* **2020**, *13*, 830–839.
- (5) Wei, Z.; Cai, C.; Huang, Y.; Wang, Y.; Fu, Y. Biomimetic Surface Strategy of Spectrum-Tailored Liquid Metal via Blackbody Inspiration for Highly Efficient Solar Steam Generation, Desalination, and Electricity Generation. *Nano Energy* **2021**, *86*, No. 106138.
- (6) Zhang, C.; Yuan, B.; Liang, Y.; Yang, L.; Bai, L.; Yang, H.; Wei, D.; Wang, W.; Chen, H. Solar Vapor Generator: A Natural All-In-One 3D System Derived from Cattail. *Sol. Energy Mater. Sol. Cells* **2021**, 227, No. 111127.
- (7) Lu, Y.; Fan, D.; Xu, H.; Min, H.; Lu, C.; Lin, Z.; Yang, X. Implementing Hybrid Energy Harvesting in 3D Spherical Evaporator

- for Solar Steam Generation and Synergic Water Purification. Solar RRL 2020, 4, No. 2000232.
- (8) Wang, S.; Fan, Y.; Wang, F.; Su, Y.; Zhou, X.; Zhu, Z.; Sun, H.; Liang, W.; Li, A. Potentially Scalable Fabrication of Salt-Rejection Evaporator Based on Electrogenerated Polypyrrole-Coated Nickel Foam for Efficient Solar Steam Generation. *Desalination* **2021**, 505, No. 114982.
- (9) Li, Z.; Ma, X.; Chen, D.; Wan, X.; Wang, X.; Fang, Z.; Peng, X. Polyaniline-Coated MOFs Nanorod Arrays for Efficient Evaporation-Driven Electricity Generation and Solar Steam Desalination. *Adv. Sci.* **2021**, No. 2004552.
- (10) Liu, K.; Zhang, W.; Cheng, H.; Luo, L.; Wang, B.; Mao, Z.; Sui, X.; Feng, X. A Nature-Inspired Monolithic Integrated Cellulose Aerogel-Based Evaporator for Efficient Solar Desalination. *ACS Appl. Mater. Interfaces* **2021**, *13*, 10612–10622.
- (11) Li, J.; Wang, X.; Lin, Z.; Xu, N.; Li, X.; Liang, J.; Zhao, W.; Lin, R.; Zhu, B.; Liu, G.; Zhou, L.; et al. Over 10 kg m⁻² h⁻¹ Evaporation Rate Enabled by a 3D Interconnected Porous Carbon Foam. *Joule* **2020**, *4*, 928–937.
- (12) Xu, N.; Li, J.; Wang, Y.; Fang, C.; Li, X.; Wang, Y.; Zhou, L.; Zhu, B.; Wu, Z.; Zhu, S.; Zhu, J. A Water Lily—Inspired Hierarchical Design for Stable and Efficient Solar Evaporation of High-Salinity Brine. Sci. Adv. 2019, 5, No. eaaw7013.
- (13) Zhang, C.; Shi, Y.; Shi, L.; Li, H.; Li, R.; Hong, S.; Zhuo, S.; Zhang, T.; Wang, P. Designing A Next Generation Solar Crystallizer for Real Seawater Brine Treatment with Zero Liquid Discharge. *Nat. Commun.* **2021**, *12*, No. 998.
- (14) Wu, X.; Wang, Y.; Wu, P.; Zhao, J.; Lu, Y.; Yang, X.; Xu, H. Dual-Zone Photothermal Evaporator for Antisalt Accumulation and Highly Efficient Solar Steam Generation. *Adv. Funct. Mater.* **2021**, *31*, No. 2102618.
- (15) Wang, Y.; Wu, X.; Gao, T.; Lu, Y.; Yang, X.; Chen, G. Y.; Owens, G.; Xu, H. Same Materials, Bigger Output: A Reversibly Transformable 2D–3D Photothermal Evaporator for Highly Efficient Solar Steam Generation. *Nano Energy* **2021**, *79*, No. 105477.
- (16) Li, N.; Qiao, L.; He, J.; Wang, S.; Yu, L.; Murto, P.; Li, X.; Xu, X. Solar-Driven Interfacial Evaporation and Self-Powered Water Wave Detection Based on an All-Cellulose Monolithic Design. *Adv. Funct. Mater.* **2021**, *31*, No. 2008681.
- (17) Zhou, X.; Guo, Y.; Zhao, F.; Yu, G. Hydrogels as An Emerging Material Platform for Solar Water Purification. *Acc. Chem. Res.* **2019**, 52, 3244–3253
- (18) Guo, Y.; Yu, G. Engineering Hydrogels for Efficient Solar Desalination and Water Purification. *Acc. Mater. Res.* **2021**, *2*, 374–384.
- (19) Li, F.; Li, N.; Wang, S.; Qiao, L.; Yu, L.; Murto, P.; Xu, X. Self-Repairing and Damage-Tolerant Hydrogels for Efficient Solar-Powered Water Purification and Desalination. *Adv. Funct. Mater.* **2021**, No. 2104464.
- (20) Zhou, X.; Zhao, F.; Guo, Y.; Zhang, Y.; Yu, G. A Hydrogel-Based Antifouling Solar Evaporator for Highly Efficient Water Desalination. *Energy Environ. Sci.* **2018**, *11*, 1985–1992.
- (21) Lu, Y.; Fan, D.; Wang, Y.; Xu, H.; Lu, C.; Yang, X. Surface Patterning of Two-Dimensional Nanostructure-Embedded Photo-thermal Hydrogels for High-Yield Solar Steam Generation. *ACS Nano* **2021**, *15*, 10366–10376.
- (22) Guo, Y.; Lu, H.; Zhao, F.; Zhou, X.; Shi, W.; Yu, G. Biomass-Derived Hybrid Hydrogel Evaporators for Cost-Effective Solar Water Purification. *Adv. Mater.* **2020**, *32*, No. 1907061.
- (23) Guo, Y.; Zhao, F.; Zhou, X.; Chen, Z.; Yu, G. Tailoring Nanoscale Surface Topography of Hydrogel for Efficient Solar Vapor Generation. *Nano Lett.* **2019**, *19*, 2530–2536.
- (24) Sun, P.; Zhang, W.; Zada, I.; Zhang, Y.; Gu, J.; Liu, Q.; Su, H.; Pantelic, D.; Jelenkovic, B.; Zhang, D. 3D-Structured Carbonized Sunflower Heads for Improved Energy Efficiency in Solar Steam Generation. ACS Appl. Mater. Interfaces 2020, 12, 2171–2179.
- (25) Yang, L.; Chen, G.; Zhang, N.; Xu, Y.; Xu, X. Sustainable Biochar-Based Solar Absorbers for High-Performance Solar-Driven

- Steam Generation and Water Purification. ACS Sustainable Chem. Eng. 2019, 7, 19311–19320.
- (26) Li, J.; Zhou, X.; Mu, P.; Wang, F.; Sun, H.; Zhu, Z.; Zhang, J.; Li, W.; Li, A. Ultralight Biomass Porous Foam with Aligned Hierarchical Channels as Salt-Resistant Solar Steam Generators. ACS Appl. Mater. Interfaces 2020, 12, 798–806.
- (27) Fang, Q.; Li, T.; Chen, Z.; Lin, H.; Wang, P.; Liu, F. Full Biomass-Derived Solar Stills for Robust and Stable Evaporation to Collect Clean Water from Various Water-Bearing Media. *ACS Appl. Mater. Interfaces* **2019**, *11*, 10672–10679.
- (28) Cao, S.; Rathi, P.; Wu, X.; Ghim, D.; Jun, Y.-S.; Singamaneni, S. Cellulose Nanomaterials in Interfacial Evaporators for Desalination: A "Natural" Choice. *Adv. Mater.* **2021**, *33*, No. 2000922.
- (29) He, S.; Chen, C.; Kuang, Y.; Mi, R.; Liu, Y.; Pei, Y.; Kong, W.; Gan, W.; Xie, H.; Hitz, E.; Jia, C.; et al. Nature-Inspired Salt Resistant Bimodal Porous Solar Evaporator for Efficient and Stable Water Desalination. *Energy Environ. Sci.* **2019**, *12*, 1558–1567.
- (30) Kuang, Y.; Chen, C.; He, S.; Hitz, E. M.; Wang, Y.; Gan, W.; Mi, R.; Hu, L. A High-Performance Self-Regenerating Solar Evaporator for Continuous Water Desalination. *Adv. Mater.* **2019**, 31, No. 1900498.
- (31) D'Arrigo, G.; Navarro, G.; Di Meo, C.; Matricardi, P.; Torchilin, V. Gellan Gum Nanohydrogel Containing Anti-Inflammatory and Anti-Cancer Drugs: A Multi-Drug Delivery System for A Combination Therapy in Cancer Treatment. *Eur. J. Pharm. Biopharm.* **2014**, *87*, 208–216.
- (32) Bacelar, A. H.; Silva-Correia, J.; Oliveira, J. M.; Reis, R. L. Recent Progress in Gellan Gum Hydrogels Provided by Functionalization Strategies. *J. Materi. Chem. B* **2016**, *4*, 6164–6174.
- (33) Osmałek, T.; Froelich, A.; Tasarek, S. Application of Gellan Gum in Pharmacy and Medicine. *Int. J. Pharm.* **2014**, *466*, 328–340.
- (34) Das, M.; Giri, T. K. Hydrogels based on Gellan Gum in Cell Delivery and Drug Delivery. *J. Drug Delivery Sci. Technol.* **2020**, *56*, No. 101586.
- (35) Morris, E. R.; Nishinari, K.; Rinaudo, M. Gelation of Gellan—A Review. *Food Hydrocolloids* **2012**, *28*, 373—411.
- (36) Saha, D.; Bhattacharya, S. Hydrocolloids as Thickening and Gelling Agents in Food: A Critical Review. *J. Food Sci. Technol.* **2010**, 47, 587–597.
- (37) Zhang, Y.; Dong, B.; Chen, A.; Liu, X.; Shi, L.; Zi, J. Using Cuttlefish Ink as An Additive to Produce Non-Iridescent Structural Colors of High Color Visibility. *Adv. Mater.* **2015**, *27*, 4719–4724.
- (38) Mendelsohn, J.; Howley, P. M.; Israel, M. A.; Gray, J. W.; Thompson, C. B. *The Molecular Basis of Cancer E-Book*; Elsevier Health Sciences, 2014.
- (39) Karthika, J.; Vishalakshi, B. Novel Stimuli Responsive Gellan Gum-Graft-Poly (DMAEMA) Hydrogel as Adsorbent for Anionic Dye. *Int. J. Biol. Macromol.* **2015**, *81*, 648–655.
- (40) Schmaler-Ripcke, J.; Sugareva, V.; Gebhardt, P.; Winkler, R.; Kniemeyer, O.; Heinekamp, T.; Brakhage, A. A. Production of Pyomelanin, A Second Type of Melanin, via the Tyrosine Degradation Pathway in *Aspergillus Fumigatus*. *App. Environ. Microbiol.* **2009**, *75*, 493–503.